ChemPubSoc Europe

DOI: 10.1002/cctc.201900618

CHEMCATCHEM Full Papers

Insight into the Role of Water on the Methylation of Hexamethylbenzene in H-SAPO-34 from First Principle Molecular Dynamics Simulations

Simon Bailleul,[a] Sven M. J. Rogge,[a] Louis Vanduyfhuys,[a] and Veronique Van Speybroeck*[a]

The methylation of hexamethylbenzene with methanol is one of the key reactions in the methanol-to-olefins hydrocarbon pool reaction cycle taking place over the industrially relevant H-SAPO-34 zeolite. This methylation reaction can occur either via a concerted or via a stepwise mechanism, the latter being the preferred pathway at higher temperatures. Herein, we systematically investigate how a complex reaction environment with additional water molecules and higher concentrations of Brønsted acid sites in the zeolite impacts the reaction mechanism. To this end, first principle molecular dynamics simulations are performed using enhanced sampling methods to characterize the reactants and products in the catalyst pores and to construct the free energy profiles. The most prominent effect of the dynamic sampling of the reaction path is the stabilization of the product region where water is formed, which can either move freely in the pores of the zeolite or be stabilized through hydrogen bonding with the other protic molecules. These protic molecules also stabilize the deprotonated Brønsted acid site, created due to the formation of the heptamethylbenzenium cation, via a Grotthuss-type mechanism. Our results provide fundamental insight in the experimental parameters that impact the methylation of hexamethylbenzene in H-SAPO-34, especially highlighting and rationalizing the crucial role of water in one of the main reactions of the aromatics-based reaction cycle.

1. Introduction

The depleting oil reserves and growing environmental awareness incites the development of sustainable processes based on biomass valorization for the production of fuels and chemicals.[1–4] As methanol can be produced from any gasifiable carbon-rich source, the methanol-to-olefins (MTO) process is one of the main technologies to bypass the use of crude oil in the production of highly demanded ethene and propene.[5–10] In particular the chabazite structured H-SAPO-34 is of industrial interest due to its high selectivity to light olefins.[11–13] Decreasing the particle size,[14–17] creating mesopores[18] or adding water[13,19–23] all improve the stability of the catalyst. Especially the influence of water on the process is highly relevant, as it is an inherent byproduct of the methanol production[24–26] and produced in the equilibration of the MTO process, as depicted schematically in Figure 1a.[27] Furthermore, early and recent

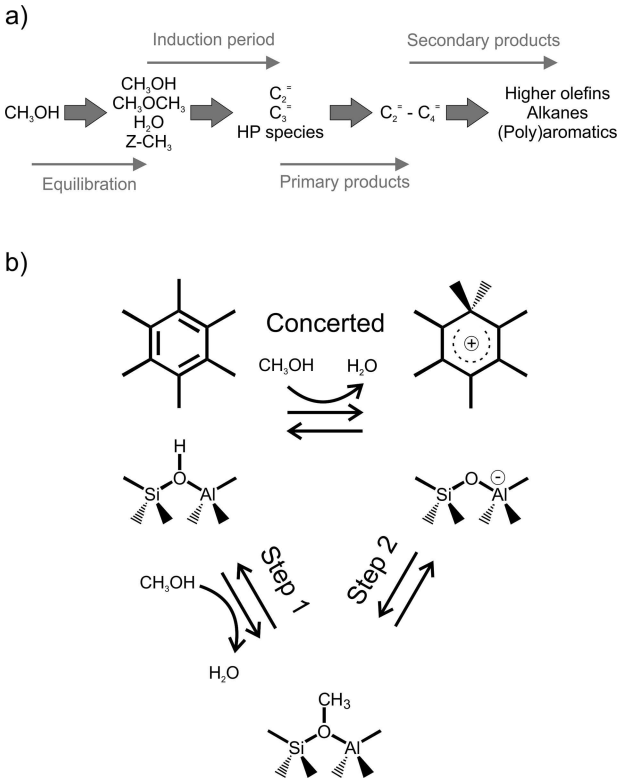

Figure 1. Schematic representation of the different stages encountered during the methanol-to-olefins (MTO) process (a) and of the mechanisms suggested for the zeolite-catalyzed hexamethylbenzene (HMB) methylation reaction, namely the direct and stepwise mechanism (b). Figure 1b was adapted from ref. [44] with permission from The Royal Society of Chemistry.[27,44]

[a] S. Bailleul, Dr. S. M. J. Rogge, Dr. L. Vanduyfhuys, Prof. V. Van Speybroeck
Center for Molecular Modeling (CMM)
Ghent University
Technologiepark 46
Zwijnaarde B-9052 (Belgium)
E-mail: veronique.vanspeybroeck@ugent.be

Supporting information for this article is available on the WWW under https://doi.org/10.1002/cctc.201900618

This manuscript is part of the Special Issue dedicated to the Women of Catalysis.

studies also demonstrated an increased olefin selectivity and decreased coking rates upon increasing the water content, effects which were assigned to competitive adsorption of water on the Brønsted acid sites (BAS), thus making them unavailable for methanol to react.[13,19,20]

Despite being commercialized, the MTO process still draws a lot of attention from both academia and industry due to its complex reaction mechanism.[8–10,28,29] Intensive research performed in the last decades to elucidate the complex MTO reaction mechanism led to the general acceptance of the hydrocarbon pool (HP) mechanism. In this mechanism, an organic compound that is trapped in the catalyst pores acts as a co-catalyst.[27,30–33] Different organic compounds are suggested as co-catalysts in literature, from which the polymethylbenzenes are identified as the dominant HP species in H-SAPO-34.[14] Especially the methylation reactions of these polymethylbenzenes are determined to be important reaction steps in the HP reaction mechanism.[34,35] A joint experimental and theoretical study has emphasized the relevance of this reaction.[36,37] They found that the band at 400 nm of the in situ UV/Vis microscopy measurements could be assigned to polymethylbenzenes. Furthermore, the activation energies derived from the growth of this characteristic peak correlated well with the activation energy for methylation of the benzenic species.

Two different routes are suggested in literature for the methylation reaction. This reaction may occur either via a concerted mechanism in which methanol transfers its methyl group directly towards the aromatic or via a stepwise mechanism, both represented in Figure 1b. In this stepwise mechanism, methanol first reacts with the catalyst framework, forming a methoxide species, which then transfers its methyl group to the HP species.[38–44] Literature suggests that both mechanisms occur within the zeolite and the prevailing mechanism largely depends on the topology and the operating conditions.[40–49] The studies show that with increasing temperature and decreasing pressure the prevailing mechanism shifts from concerted to stepwise.[45] This effect is attributed to the entropic gain of the intermediate release of water during the stepwise mechanism.[43,44,47]

The temperature and entropic effects make this reaction especially interesting to demonstrate the importance of a good description of the reaction conditions and entropic contributions using dynamic methods instead of static modeling techniques. Recent theoretical modeling work is more and more focused on the use of molecular dynamic (MD) techniques.[13,28,50–55] Nevertheless, regular MD simulations have the disadvantage of mainly sampling the most probable regions of the phase space making the elementary reactions that are interesting in most reaction mechanism rare events and thus difficult to examine. This hurdle can be overcome via enhanced sampling methods that steer the system to cross the reaction barrier.[56] Several of these free energy methods are already reviewed in literature.[56–60] In this paper, metadynamics (MTD)[61–63] and umbrella sampling (US)[64–66] are used to study the reaction under consideration. Both free energy methods, also referred to as non-Boltzmann sampling methods, use controlled bias potentials to enhance the sampling of the configurational space.[56] The main difference between both techniques is that, while the bias potentials used in umbrella sampling need to be chosen and constructed at the beginning of the simulations, metadynamics has the advantage of building a bias potential on-the-fly during an MD simulation.

In this work, we want to obtain insight into one of the main steps – the methylation reaction – of the operative cycle in H-SAPO-34 and the influence of water on it, as the intermediate removal of the water molecule is suggested to be of great importance[43,44] and co-feeding of water showed significant influence on the product selectivity and catalyst lifetime.[13,19,20] To mimic as closely as possible realistic operating conditions during the MTO process, three cases are investigated in this work, depicted in Figure 2. Firstly, an isolated Brønsted acid site (BAS) with one hexamethylbenzene (HMB) molecule and one methanol is considered as the base case (Case 1). This base case will be used to compare the advanced MD techniques with the static results, which will allow us to study the influence of the computational methodology and to highlight the importance of a good description of the diffusional freedom of water. Subsequently, we create a more complicated and realistic representation of the catalyst pores. To this end, two adaptations to the system are considered. First of all, one additional methanol molecule and either one or nine adsorbed water molecules were added for Case 2 and Case 3, respectively, as earlier studies show that these protic molecules might interact to form protonated clusters, which decreased the reactivity.[67] This maximum water loading at operating conditions was estimated using an in-house developed thermodynamic model for the adsorption of guest species in nanoporous materials.[13,68] Furthermore, there is quite some experimental work available on how the water loadings depend on the acid site density, water vapor pressure and temperature in H-ZSM-5 and for which some interesting analogies can be found with our work.[69–73] Secondly, as there is a high probability to find two silicon atoms in the next nearest neighbor position in SAPO materials, we introduced a second acid site in the unit cell,[74,75] as was done in our earlier work.[36,52] Note that the schematic representation shown in Figure 2 corresponds to starting structures. During the simulations the system adopts more realistic configurations in the pores of the material (*vide infra*). Thanks to these adaptations, the conclusions of Case 1 can be generalized to experimentally more realistic pore environments and the influence of the assisting effect of additional protic molecules on both methylation mechanisms can be assessed.[13,41,44] For the system under study, molecular dynamics methods are of utmost importance to properly account for the dynamic interplay between the methylating agent, hexamethylbenzene and water.

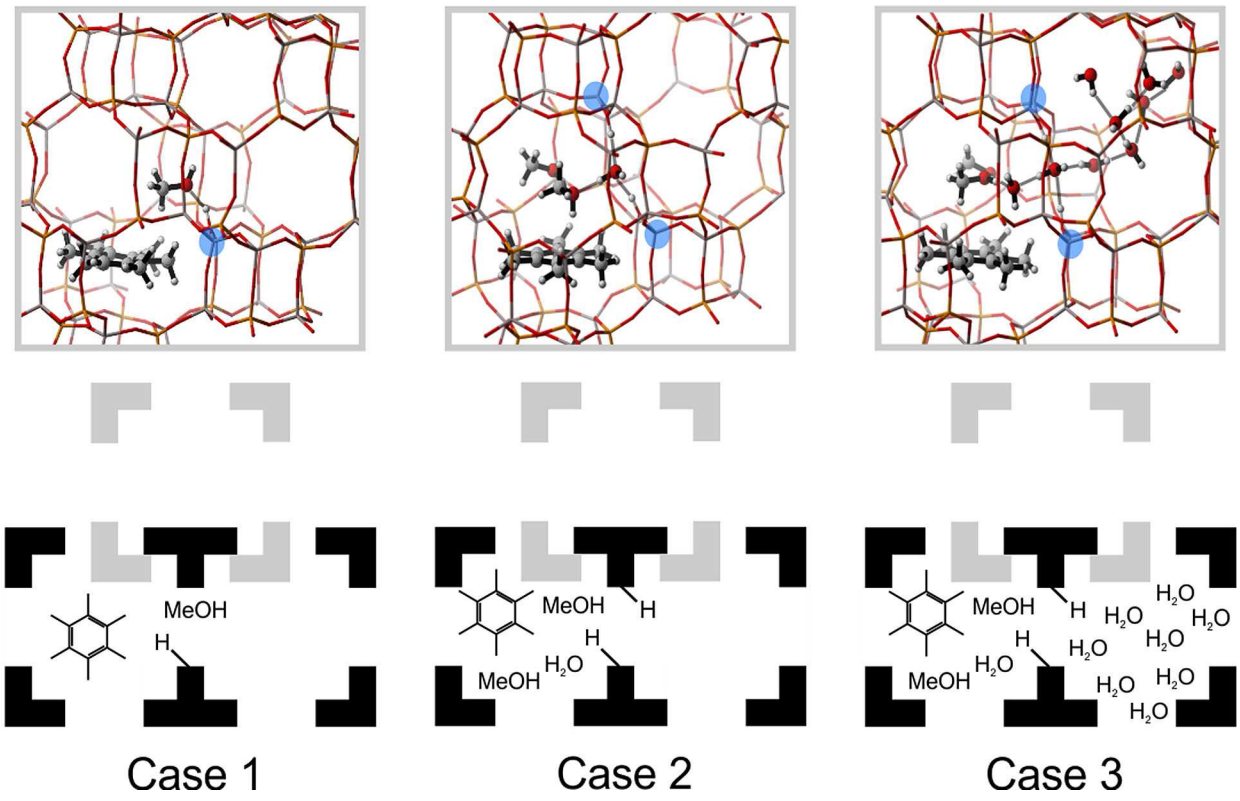

Figure 2. Starting structures and schematic representations of the three cases considered to study the concerted and stepwise methylation of HMB, namely an isolated BAS with one HMB and one methanol as base case (Case 1), a more realistic low water content case (Case 2) and high water content case (Case 3). In these snapshots, hydrogen is white, carbon is silver, oxygen is red, aluminum is grey, the silicon substitution is indicated in blue and phosphorus is orange.

2. Computational Methodology

2.1. Catalyst Model and Water Loading

Due to its commercial importance for the MTO reaction,[11] this study focuses on the H-SAPO-34 framework. This zeotype catalyst exhibits the CHA topology, which consists of large cages (10.0×6.7 Å^2) connected via small windows (3.8×3.8 Å^2).[76] In contrast to the finite cluster models which are used in some earlier studies,[12] density functional theory (DFT) calculations are applied on periodic catalyst models in this work. Therefore, a unit cell of 36T atoms (see Figure S1 in ESI) that contains one Brønsted acid site (BAS) on the O(2) position to make the catalyst active for reaction is used to represent the catalyst framework for the base case (Case 1).[77] This unit cell is shown in detail in Figure S1c. Furthermore, as there is a high probability to find two silicon atoms in the next nearest neighbor position in SAPO materials, we introduced a second acid site in the unit cell for Cases 2 and 3,[74,75] as shown in Figure S1d.[36,52]

As described in the introduction, additional water molecules were added in Case 2 and 3 respectively. To rationalize the proposed water loading in the various cases investigated in this work, we estimated the water loading using an in-house developed thermodynamic model for the adsorption of guest species in nanoporous materials.[13,68] This model allows one to estimate the number of adsorbed water molecules inside the zeolite as a function of the chemical potential of water given the adsorption energy of water, the accessible pore volume of the framework and the van der Waals parameters of water. More details on this thermodynamic model can be found in Section 1.2 of the ESI. The adsorption enthalpy was taken from literature as −42 kJ/mol.[69,78] Olson et al.[69] found that the isosteric heats of adsorption are dependent on the water content, but varies from a high value of −105 kJ/mol at low water loading to −42 kJ/mol a higher water loading. Furthermore, from earlier theoretical calculations, an adsorption enthalpy of −75 kJ/mol was found.[13] The previous values may be prone to some uncertainties both from theoretical and experimental point of view, but the adsorption enthalpy taken as input for our thermodynamic analysis is the lower limit of −42 kJ/mol. The pore volume was calculated using Zeo++ to be 1250 Å^3.[79] To account for the space occupied by hexamethylbenzene and the two methanol molecules already present in the pores, we subtracted from the total pore volume the van der Waals volume of these molecules (i.e. its van der Waals *b* parameter). For methanol, this value was taken directly from ref. [80] (b_{CH3OH} = 109 Å^3), while for HMB this value was extrapolated from the benzene, toluene, xylene, trimethylbenzene and tetramethylbenzene values also taken from ref. [80] (b_{HMB} = 493 Å^3). As such, we arrive at an accessible pore volume of 538 Å^3. Finally, the van der Waals parameters of water (a_{H2O} =

919 kJ/(mol.Å^3) and b_{H2O} = 50.6 Å^3) were taken from ref. [80] After applying the model for a temperature of 623 K and a water partial pressure of 0.8 atm[19,23] we finally arrive at an equilibrium loading of 8.6 water molecules per unit cell at these thermodynamic conditions. As each unit cell consists of three cages (schematically depicted in Figure 2), where one cage contains the HMB, the additional water molecules can be accommodated in the other two cages. To further test the dependency of this water loading content, we tested in how far the water loading depends on the adsorption energy and vapor pressure. Only for very low vapor pressures (below 0.06 atm) or very low adsorption energies (lower than −25 kJ/mol), the loading would drop drastically. More information is given in section 1.2 of the ESI. Previous consideration and analysis shows that the assumed water content is a reasonable estimate, however the true water content may be dependent on the pore volume and other process condition factors. In this sense the assumed loading here should merely be interpreted as a rough but realistic estimate and a limiting case. More advanced models, for instance relying on grand canonical Monte Carlo simulations to estimate the adsorption isotherms at operating conditions, are out of the scope of this study.[81,82]

The unit cell parameters used to describe the H-SAPO-34 framework depend on the calculation method and guest loading, as statically the unit cell parameters are calibrated for the empty-host structure at 0 K, while the unit cell parameters for the enhanced sampling simulations are obtained at 623 K and with realistic guest loadings. The equilibration procedures are described in Section 1.1.2 of the ESI and the resulting unit cell parameters are summarized in Table S1 (ESI).

2.2. Static Calculations

The static periodic DFT calculations are performed using the Vienna Ab Initio Simulation Package (VASP 5.3)[83–86] using a methodology frequently applied in literature.[87–90] We here opted to use the revPBE functional due to its improved performance for solid-state calculations compared to the commonly used PBE functional.[91] However, for this particular reaction the differences in reaction barriers and energies are relatively small at the temperature of interest. A comparative table for the reactions of interest is taken up in Table S1, Table S7 and Table S8 of the SI. During the calculations, the projector augmented wave (PAW) method is used.[92,93] Furthermore, a plane-wave cutoff of 600 eV is used during the calculations, the self-consistent field (SCF) convergence criterion is set to 10^{-5} eV, and the Brillouin zone is restricted to the Γ-point. Lastly, Grimme D3 dispersion corrections are used to account for attractive London dispersion interactions.[94] The electronic level of theory adopted in this study is commonly used in zeolite catalysis due to its computational efficiency. Detailed level of theory studies have been performed on various zeolite catalyzed reactions, which show that barriers may be severely underestimated using the PBE-D method.[28,95–98] Seminal work was done by Sauer and co-workers to compare the accuracy of commonly used DFT methods in combination with various schemes to include the dispersion interactions. They also considered more accurate but also computationally more demanding methods which include contributions from the Møller-Plesset perturbation theory (MP2) or methods where the exact exchange is combined with correlation treated in the random phase approximation.[99–101] In addition, also hybrid functionals may be an interesting alternative.[102–105] However, as it is the intention to compare static with molecular dynamics results the usage of these computationally more expensive levels of theory is beyond current computational feasibilities.

Transition states are initially optimized with the improved dimer method of Heyden et al.[106] and then refined with a quasi-Newton algorithm as implemented in VASP.[107] Geometries are slightly displaced along the normal mode corresponding to the motion that leads the system over the barrier to generate starting geometries for the optimization of reactant and product states. For these calculations, a conjugate gradient algorithm is applied.[108]

As earlier work showed that a partial Hessian vibrational analysis (PHVA) is able to predict adsorption entropies within a 10–15 J/(mol K) error of computationally more demanding full Hessian calculations (FHVA) and experimental data,[109,110] it has become a frequently applied and attractive methodology.[87–90] For this reason, it is also used for the normal mode analysis (NMA) in this work using TAMkin.[109,111] In a PHVA calculation, not the entire system, but only a part, namely the guest molecules and the 8T cluster of the framework around the active site indicated in Figure S1c of the ESI, are accounted for during the NMA.

2.3. Ab Initio Molecular Dynamics

The ab initio MD simulations are performed using the CP2K software package.[112,113] To account for the flexibility of the catalyst framework at realistic reaction conditions, we sample in the NPT ensemble at 623 K and 1 atm. During the ab initio MD simulations, the temperature is controlled by a Nosé-Hoover chain consisting of five beads[59] and the pressure by an MTK barostat.[114] Also for these simulations, the revPBE functional is chosen because of its improved performance for solid-state calculations compared to the commonly used PBE functional.[91] Furthermore, the combined Gaussian and Plane Wave (GPW) basis sets approach is used.[115,116] The DZVP-GTH basis set and pseudopotentials[117] are used, and Grimme D3 dispersion corrections[94] are added. The time step for integration of the equations of motion is set to 0.5 fs. All systems are first equilibrated for 5 ps, followed by a production run of 50 ps. These simulation times are relatively short, due to the high computational demand for ab initio MD simulations on these periodic systems.

These first principle molecular dynamics simulations are used to study the influence of dynamically sampling the phase space on the reactant configurations visited compared to the statically obtained configurations. To compare both methodologies, the geometric analysis[44,46] described in Section 1.3 of

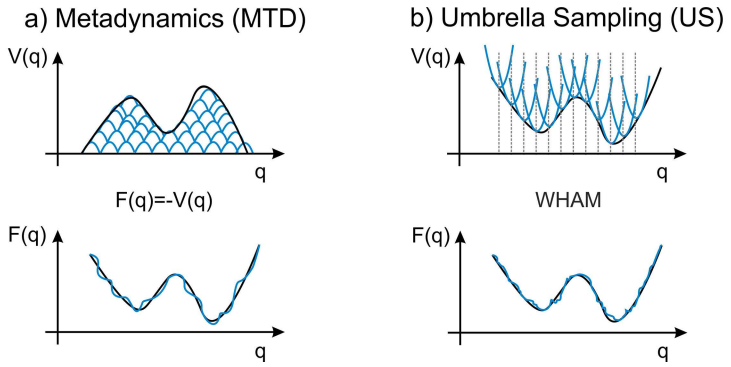

Figure 3. Schematic representation of the used enhanced sampling techniques: metadynamics (a) and umbrella sampling (b). More information on these techniques can be found in paragraph 2.4.

the ESI is performed on the static and MD simulations for Case 1 and on the MD simulations of Case 2 and Case 3.

To systematically analyze the interactions between the molecules inside the catalyst pores for all three cases considered here, radial distribution functions (RDFs) for pairs formed by key atoms of the adsorbed molecules and/or the BAS(s) of the catalyst are constructed. For all RDFs considered here, only interactions at distances below 7 Å are probed, which do not exceed halve of the smallest cell dimension to avoid spurious interactions with periodic images when using the minimum image convention.[59] The RDF analysis is carried out with YAFF starting from the MD trajectories using a resolution of 0.01 Å.[118] Besides the RDFs for the equilibrium NPT simulations in the reactant and product state, we additionally report RDFs as obtained from the non-equilibrium MTD simulations (*vide infra*). While these non-equilibrium RDFs no longer retain the property that they reveal the equilibrium distribution of the considered pairs of key atoms, they do provide information on (i) how the MTD simulation steers the reaction from the reactant to the product state and (ii) the influence of the walls used during the MTD simulations on the RDFs, which should remain negligible in all cases so not to interfere with the dynamics of the system.

2.4. Enhanced Sampling Methods

Subsequently, the influence of the reaction temperature and the water loading on the reaction profile of the direct and stepwise methylation of HMB is assessed by using metadynamics and umbrella sampling simulations, both shown schematically in Figure 3.

2.4.1. Metadynamics

In metadynamics, the system is driven over the reaction barrier by a time-dependent bias potential $V_G(q,t)$. Typically, this bias consists of a superposition of Gaussian shaped hills [Eq. (1)]:[57]

$$V_G(q,t) = w \sum_{t'=\tau_G,2\tau_G,t'<t} \exp\left(-\frac{(q-q(t'))^2}{2\delta s^2}\right) \quad (1)$$

where w, δs and τ_G are the height of, the width of and the time interval between two spawn Gaussian hills, respectively. The basic assumption of MTD is that in the limit of a sufficiently long simulation time, the bias potential is related to the free energy via Equation (2):[57,61,62]

$$\lim_{t\to\infty} V_G(q,t) = -F(q) \quad (2)$$

Therefore, the free energy surface (FES) of the system can be reconstructed based on the inversion of the time dependent bias potential as represented schematically in Figure 3a.

The Gaussian hills are spawned along a collective variable (q). In this work, coordination numbers (*CN*) are used as the collective variables, similar to earlier work [Eq. (3)]:[44,67]

$$CN = \sum_{i,j} \frac{1-(r_{ij}/r_0)^{nn}}{1-(r_{ij}/r_0)^{nd}} \quad (3)$$

In this expression, the sum runs over two sets of atoms i and j, r_{ij} is the distance between atoms i and j, and r_0 represents the reference distance.[28] For all coordination numbers used in this study, a reference distance r_0 of 2.0 Å was chosen, because this value lies in the range of typical transition state distances of the bonds that have to be broken and formed during a methylation or methoxide formation. The parameters *nn* and *nd* are set to 6 and 12, respectively, ensuring a value of 0.5 for each CN term at the reference distance and a fast decaying value at larger distances. Quadratic walls were used to restrict the simulations to the area of interest on the FES (Section 1.4 of ESI).[44] In this way, the reacting methanol molecule is kept close to the acidic proton and the diffusion of the formed water is limited to enhance barrier recrossings. The initial height of the Gaussian potentials is set to 5 kJ/mol and after each recrossing of the transition point, the height of the added Gaussian hill is halved to enhance the FES convergence, until a value of 0.625 kJ/mol is obtained. A new hill is spawned every 50 time

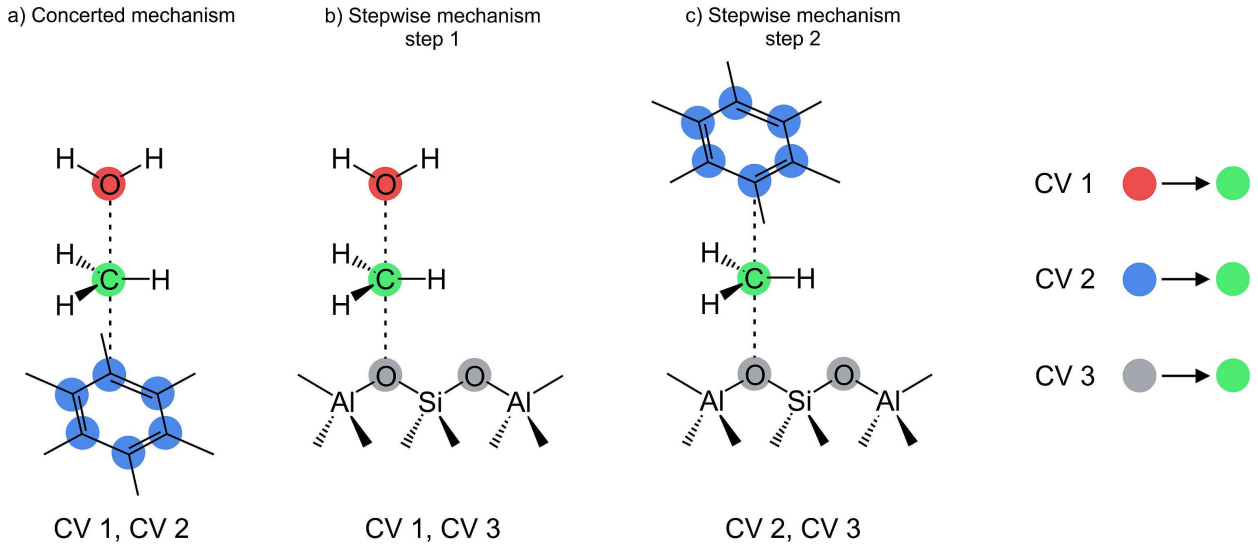

Figure 4. Schematic representation of the collective variables applied in the metadynamics and umbrella sampling simulations of the HMB methylation. [44]

steps. The width of all Gaussians is set to 0.02. The integration time step is set to 0.5 fs for all MTD simulations.

As displayed in Figure 1, three reaction steps need to be simulated to analyze both possible pathways of the methylation reaction. These reactions can all be described using the three CVs given in Figure 4.[44] The concerted methylation is characterized by the breaking of the C–O bond in methanol (CV1) and the formation of a bond between the carbon of the methyl group and one of the carbons of the aromatic ring of HMB (CV2). In the first step of the stepwise pathway, again the methanol C–O bond is broken (CV1), but now a bond is formed between the carbon of the methyl group and one of the oxygens next to the silicon substitution of the framework BAS(s) (CV3). In the second step, the formed methoxide C–O bond is broken (CV3), while the bond between the carbon of the methyl group and one of the carbons of the aromatic ring of HMB is formed (CV2).

So, each reaction can be simulated separately by combining two of the three collective variables. In principle, it is also possible to sample both mechanisms simultaneously by using the three collective variables during one metadynamics simulation,[52] but this is omitted in this work as this is computationally too expensive. It is known that the efficiency of metadynamics scales exponentially with the number of collective variables.[63] Furthermore, further work by De Wispelaere et al.[44] showed that no reaction free energies could be obtained from the 3D MTD simulations, as the product region was insufficiently sampled within feasible simulation times. One could also directly compute the 1D profiles using a single CV. However, that requires a priori knowledge on which mathematical function of the two relevant CVs represents an efficient direction to steer the reaction. Since such knowledge is not always available, metadynamics simulations are performed using two CVs, and 2D FESs are obtained. From these FESs, a free energy barrier ΔF can be computed after projection of the 2D FES onto a 1D surface, taking the difference $q = q_2 - q_1$ as the reaction coordinate [Eq. (4)]:

$$F(q) = -\frac{1}{\beta}\ln\left\{C\int_{-\infty}^{+\infty}\exp[-\beta F(q_1, q_1+q)]dq_1\right\} \quad (4)$$

where $\beta = \frac{1}{k_B T}$ with k_B the Boltzmann constant and q^* is the position at the top of the barrier along the reaction coordinate. The factor C was introduced to ensure consistent dimensions in the definition of $F(q)$ and $F(q_1, q_1+q)$ and as a result also makes sure that the argument of the logarithm is dimensionless (see Section 3.1 of the ESI for more details). However, it only results in a global shift of the free energy profile and hence does not influence free energy barriers and differences. Therefore, it is set to unity in this work.

Finally, based on the reaction rate derived from transition state theory, we can define phenomenological free energy barriers ΔF [Eq. (5)]:

$$\Delta F = F(q^*) + k_B T \ln\left(\frac{k_B T \bar{Z}_R}{hA}\right) \quad (5)$$

with k_B Boltzmann's constant, h Planck's constant and T the temperature. Furthermore, $F(q^*)$ represents the free energy of the transition state q^* (relative to the minimum in the reactant valley), $\bar{Z}_R$ is proportional to the partition function of the reactant valley and hence accounts for the broadness of the reactant valley, while the factor $A = \frac{1}{2}\langle|\dot{q}|\rangle_{q^*}$ is related to the rate of change of the collective variable in the transition state and was computed by the procedure proposed by Bučko et al.[54] More details can be found in Section 3.2 of the ESI.

The metadynamics simulations are performed using the CP2K software package.[112,113] As the change in cell parameters was found to be negligible during the methylation reaction for each of the three cases (see Table S1 (ESI)), these simulations were performed in the NVT ensemble at 623 K for computa-

tional efficiency as explained in Section 1.1.2 of the ESI. During these simulations, the temperature is again controlled by a Nosé-Hoover chain of five thermostat beads.[59] Furthermore, time-averaged cell parameters obtained from the NPT runs for each of the three cases are used as constant values. These time-averaged cell parameters are summarized in Table S1 (ESI). The remainder of the settings are kept the same as for the MD simulations described in paragraph 2.3.

2.4.2. Umbrella Sampling

During umbrella sampling, the reaction path is separated into distinct windows, as shown in Figure 3b. In each window, the reaction coordinate is restrained to a target value q_i^{ref} by applying a bias potential in each window. Often, a harmonic bias potential with strength K is used to keep the system close to the target value [Eq. (6)]:

$$w_i(q) = \frac{K}{2}(q - q_i^{ref})^2 \quad (6)$$

In each window, the system mainly samples perpendicular to the reaction coordinate. After the simulations are completed, the probability distribution of all windows is combined to a total distribution function using the weighted histogram analysis method (WHAM) to obtain the free energy surface of the unbiased system.[119,120]

The umbrella sampling simulations are performed using the CP2K software package[112,113] which is interfaced with the advanced simulations library PLUMED.[121] To keep the simulations as similar as possible to the metadynamics simulations, the settings are kept the same. The simulations are therefore performed in the NVT ensemble at 623 K. The temperature is again controlled by a Nosé-Hoover chain of five thermostat beads.[59] Again, time-averaged cell parameters obtained from the NPT runs are used as constant values as summarized in Table S1 (ESI). The remainder of the settings are kept the same as for the MD simulations described in paragraph 2.3.

The collective variables that are used to describe the analyzed reactions are the same as discussed in paragraph 2.4.1. To create the snapshots used as a starting point for each window, a moving restrained MD simulation is used in which a bias potential is moved from one minimum to the other. Along this 2000 step reaction path, a snapshot is taken every 80 steps, leading to 26 umbrellas for each reaction. Subsequently, a restrained ab initio MD simulation of 50 ps is run for each umbrella. If insufficient overlap between the different umbrellas occurred, extra umbrellas were added in the poorly sampled regions. This methodology led to the umbrellas summarized in Table S2 and Table S3 (ESI) where the location for each window is summarized. The force constant is always set to 1500 kJ/mol.

3. Results and Discussion

The concerted and stepwise methylation mechanisms are studied using both static and dynamic simulation methods.[38–42] Earlier studies have emphasized on the importance of the water released during the stepwise mechanism.[43,44] This makes this reaction especially interesting to demonstrate the importance of a good description of the entropic contributions by release of water using dynamic methods instead of static techniques. At first instance, a structural analysis of all reaction components within a realistic representation of the catalyst pores will be discussed. In the second part, the influence of the dynamic analysis and the realistic pore environment on the reaction barriers for both the concerted and the stepwise mechanisms will be discussed. We use a variety of analysis tools which will first be introduced for the simplest case, namely Case 1. Afterwards, the conclusions will be generalized to experimentally more realistic systems by expanding the analysis to Case 2 and Case 3.

3.1. Dynamic Reactant and Product Behavior

To obtain insight in the effect of the dynamic behavior and mobility of the reactants on the co-adsorption of the HP species, a geometric analysis is performed on the results of the MD simulations at 623 K. Firstly, the mobility of the HMB will be analyzed. Subsequently, the diffusive and protic behavior of methanol in the reactant state is studied. Lastly, the relative orientation of HMB and methanol will be investigated to unveil their tendency to form pre-reactive complexes.

3.1.1. Preferential Orientation of Polymethylbenzene

To analyze the mobility and orientation of the organic co-catalyst in the H-SAPO-34 framework, two angles α and β, defined in Figure S7 of the ESI, are monitored during a regular MD simulation in the reactant valley. The angle α describes the orientation of HMB along the longest axis of the cage (z-direction), where an angle close to 0° indicates that HMB is oriented parallel to the length of the cage and an angle close to 90° indicates a perpendicular orientation. The angle β is defined as the angle between the HMB and the normal of the 8T-ring of the catalyst in which the BAS(s) are found. Here, an angle close to 90° means parallel to this window and thus a favorable orientation of the π-clouds to the BAS, while an angle close to 0° means perpendicular, as visualized in Figure S8 of the ESI. The time-dependent values for these angles are calculated over the trajectory of a 50 ps MD simulation for the reactant state of all three cases and the resulting normalized histograms are depicted in Figure 5a and b. For Case 1, the static result is also included as a dotted line. Snapshots of the most probable configurations for all three cases are depicted in Figure 5c. The histograms show that in all three cases, the most probable structures obtained dynamically correspond to configurations in which α is in the range of 0°–30°. Thus, HMB orients itself

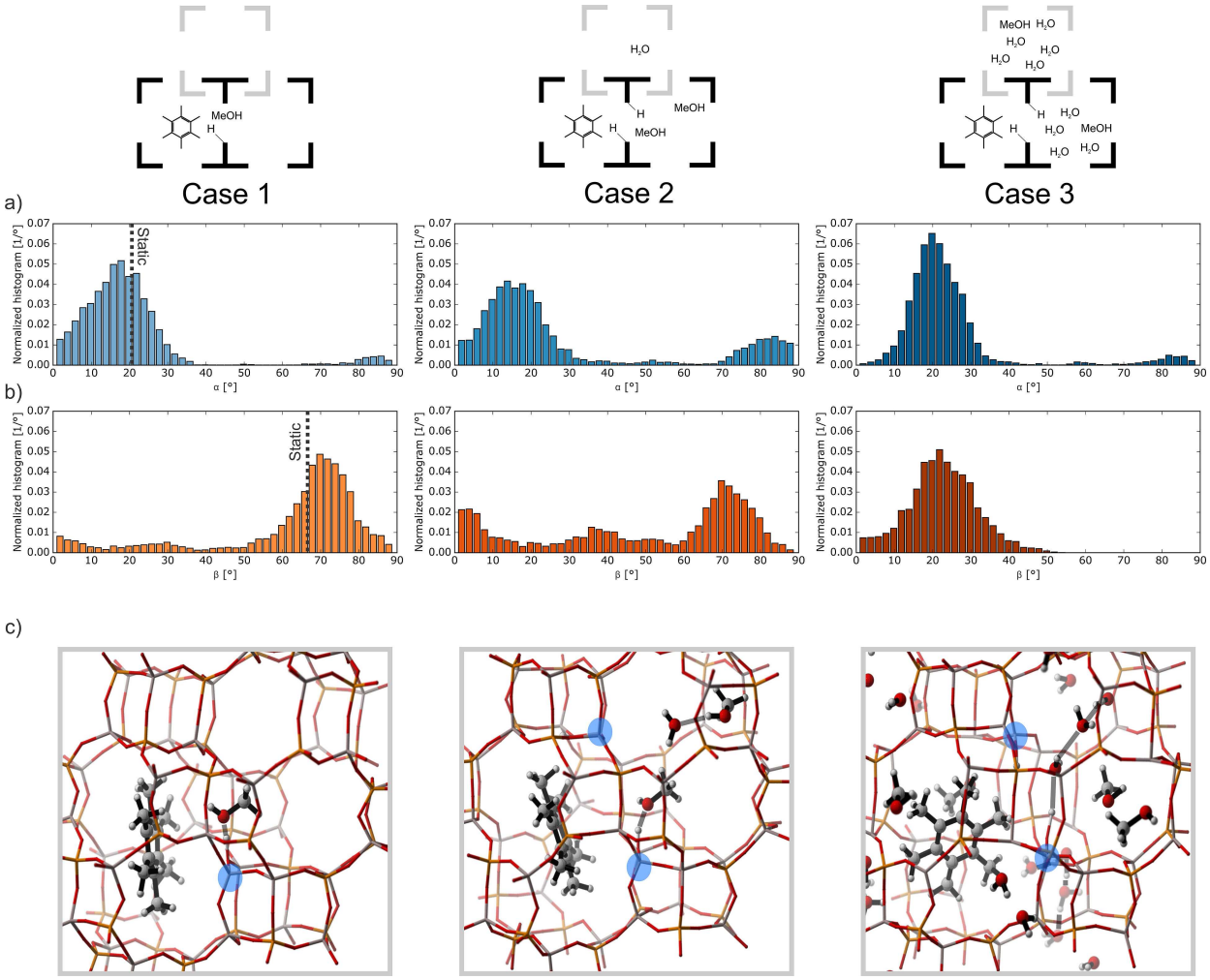

Figure 5. Summary of the geometric analysis for a 50 ps MD simulation of the reactant state of Case 1 (left), Case 2 (middle) and Case 3 (right) showing the normalized histogram for the angle α (a) and the angle β (b) defined in Section 1.3 of the ESI and snapshots showing the most probable orientation adapted by the HMB (c). The dotted line depicts the corresponding reactant structure obtained via static simulations of Case 1.

more or less parallel to the length of the cage irrespective of the starting configuration. For Case 1, also the statically obtained configuration agrees well with the dynamically obtained most probable configuration, although it neglects the width of the dynamic distribution. The angle β adopts values in the range of 70°–90° in Case 1, as in this orientation the π-clouds orient themselves towards the BAS. Also for Case 2, the largest contribution of β is found in the same range, although the histograms show a slightly higher contribution at other values. These residual contributions at other values originate from the chosen input structures as depicted in Figure 2. The HMB reorients itself towards the most favorable configuration during the course of the MD run. However, due to the presence of more guest molecules this goes slightly slower in Case 2 compared to 1. In Case 3 the most probable configuration of HMB corresponds to β values in the range of 15°–30°, while the HMB molecule still orients itself along the z-axis for Case 3 ($\alpha \approx 20°$). In this case the preferential orientation of the π-clouds towards the BASs is lost. This can be understood since the additional protic molecules in Case 3 both screen the BAS and offer new stabilizing interactions for the π-clouds through the other 8-ring windows, such that the HMB no longer needs to orient its π-clouds towards the 8-ring containing the BASs.

3.1.2. Diffusive and Protic Behavior of Methanol and Water

Further insight in the early stages of the methylation process can be obtained by analyzing the mobility and orientation of the methanol. Since it is well known that methanol needs to be protonated to be active for the methylation reaction, the interaction of methanol with the protons present in the catalyst pores is studied.[67] To this end, the RDFs for the pairs formed by (i) the oxygen of methanol and (ii) all protons present, depicted in Figure 6, are discussed. The RDF of Case 1 shows two interesting peaks, which correspond to the O–H covalent bond of methanol itself (around 1.0 Å) and the O–H hydrogen bond with the proton of the Brønsted acid site, as schematically

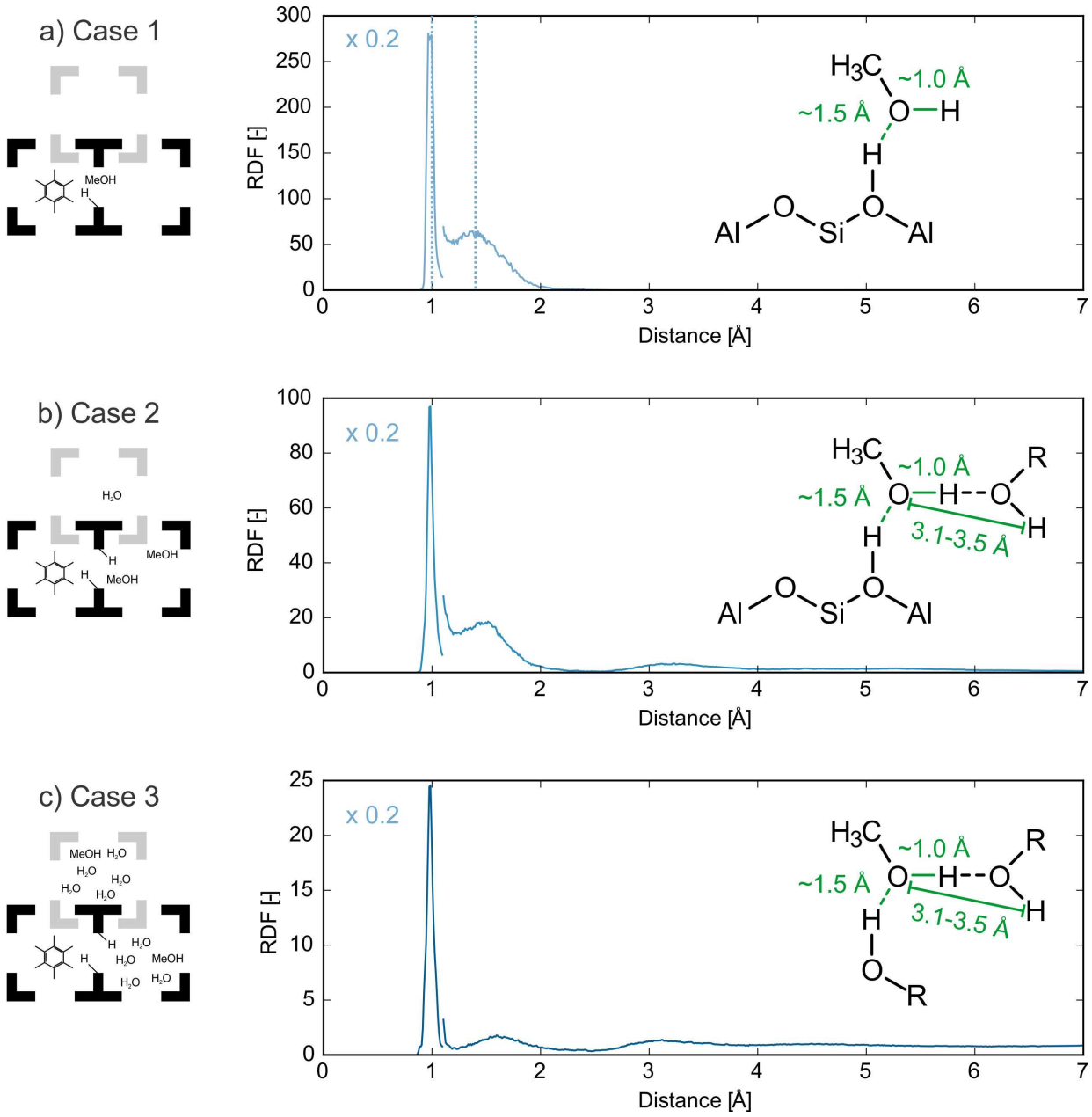

Figure 6. Radial distribution functions for the pairs formed by (i) all protons present in the catalyst pore and (ii) the oxygens of the methanol molecule(s) in the reactant state for Case 1 (a), Case 2 (b) and Case 3 (c). For Case 1, the statically obtained distances corresponding to the analyzed bonds are added in dotted lines. The encountered peaks are indicated on the schematic representation of the methanol molecule. The first peaks (at distances below about 1.1 Å) are scaled down by a factor of 5 to improve visualization.

indicated in Figure 6. The presence of this hydrogen bond peak indicates that methanol adsorbs quite localized on the BAS in Case 1. These two peaks correspond very well with the corresponding distances obtained from the statically optimized reactant state, indicated by the dotted lines in the top RDF. These peaks and bond types remain present in the more complicated Case 2 and Case 3. However, an additional peak between 3.1 and 3.5 Å arises at this more complex reaction environment. This peak is attributed to the formation of a first solvation shell around the methanol, as this distance corresponds to the distance between the oxygen of methanol and the hydrogens of a protic molecule – either water or methanol – which is hydrogen bonded to this methanol, as indicated in the middle and bottom panel of Figure 6. In Case 3, this solvation effect becomes even more prominent, since the relative intensity of this peak increases. As protonated clusters consisting of protic molecules and the protonated BAS can be formed in this case, the proton donation to the methanol can also occur through another protic molecule instead of directly from the framework. Similar results were found for the solvation shells around water as discussed in Figure S24 of the ESI.

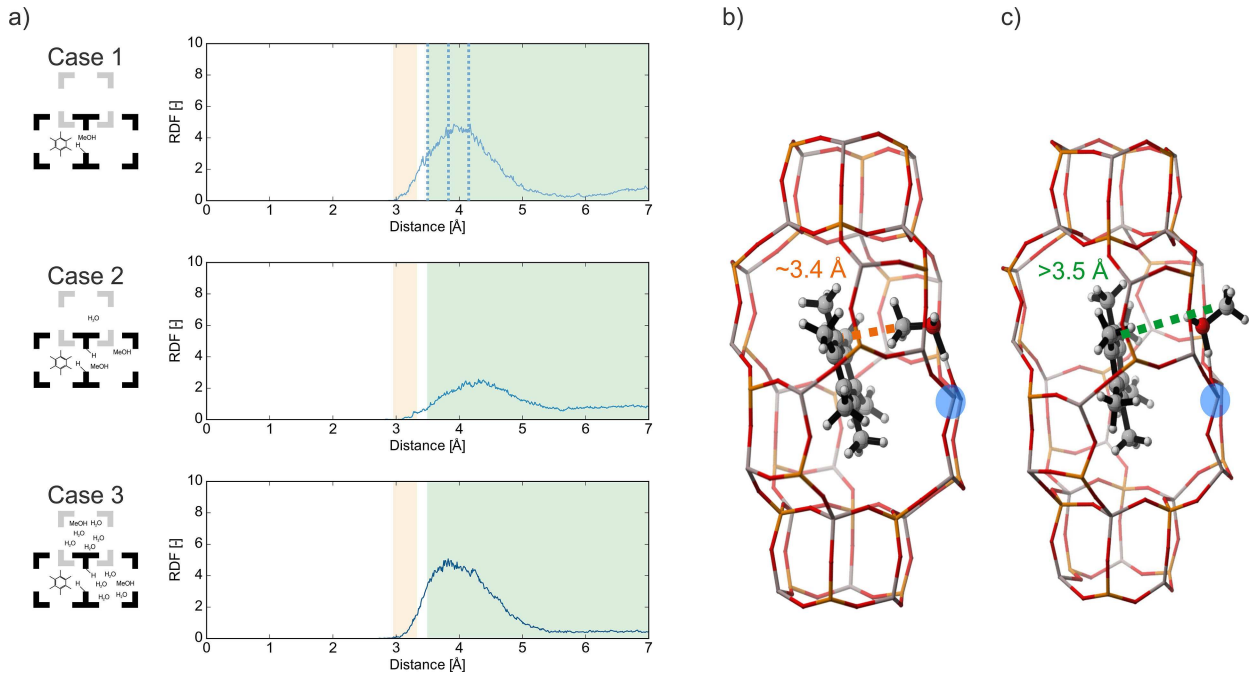

Figure 7. Radial distribution functions for the pairs formed by (i) the methyl group of the methanol molecule(s) and (ii) the carbon atoms of the benzene ring of the hexamethylbenzene molecule in the reactant state for the three cases (a). These RDFs show that the formation of a pre-reactive complex for the concerted methylation (b and orange zone in a) with a C–C distance of around 3.4 Å is rather unlikely. Instead, configurations where the methyl group of methanol is not oriented towards the aromatic ring (c and green zone in a), with distances ranging from 3.5 Å and higher, are sampled. The snapshots are obtained by static optimizations. In these snapshots, hydrogen is white, carbon is silver, oxygen is red, aluminum is grey, the silicon substitution is indicated in blue and phosphorus is orange.

3.1.3. Pre-Reactive Complexes

To have a favorable reactive environment for the methylation reaction, not only the separate orientation and movement of both adsorbed molecules with respect to the catalyst pore is important, but also a favorable position and orientation between methanol and HMB is necessary for the methylation to take place. To this end, the RDF for the pairs formed by (i) the carbon of methanol and (ii) the carbons of the aromatic ring of HMB are calculated, as depicted in Figure 7a. To form a pre-reactive complex, the methyl group of the methanol molecule should orient itself towards the HMB molecule. For Case 1, the RDF shows a broad peak around 4.0 Å. However, typical distances occurring within a pre-reactive complex optimized statically amount to only around 3.4 Å, as shown in Figure 7b. Hence, rather high methyl-HMB distances are sampled, corresponding with methanol pointing away from the aromatic ring as for the snapshot in Figure 7c. As the most stable statically obtained structure also resembles the structure in Figure 7c, good correspondence is obtained between the static distances and the RDF obtained dynamically for Case 1. Case 2 and 3 provide in general terms a rather similar picture, although some subtle differences are noted. The RDF peak for Case 3 is shifted to slightly lower values compared to Case 2, which is due to the additional guest molecules present rather than an enhanced probability to form a pre-reactive complex. The increased filling of the cages with water pushes the methanol closer to HMB.

By combining all observations from this section, we can conclude that although the HMB is oriented favorably towards the BAS and methanol can frequently interact with a second proton, the unfavorable orientation of methanol with respect to the aromatic ring limits the reactivity for the methylation reaction. To increase the likelihood of HMB methylation, it is therefore a prerequisite to use enhanced sampling techniques. Further insight into the effect of water on the reactivity for methylation will thus be obtained by calculating the methylation barriers using different methodologies in the next section.

3.2. Influence of Water on the Reaction Free Energy Profile

To unravel the full reaction mechanism, not only insight into the dynamic behavior of the reactant state is necessary, but also information on the free energy barrier and reaction free energy is indispensable. Therefore, this section will describe the influence of a dynamic description of the pore environment and the realistic filling of the catalyst pores on this barrier obtained for both the concerted and stepwise methylation mechanisms. A summary of all obtained barriers can be found in Table 1. In addition, we also performed an error analysis according to a procedure described in Section 1.6 of the SI. The error bars are also reported in Table S4 and Table S5. Before discussing in depth the numerical results, it is important to acknowledge that obtaining accurate free energies from

Table 1. - Free energy at 623 K for the concerted and stepwise methylation of HMB obtained with different methodologies, namely statically, via metadynamics (MTD) or umbrella sampling (US) (in kJ/mol). $\Delta F^{\neq}$ is used for the free energy barrier, while ΔF_r shows the reaction free energy and $\Delta G_{r,des}$ for the reaction free enthalpy after desorption of the formed water.

		Concerted			Step 1			Step 2		
		$\Delta F^{\neq}$	ΔF_r	$\Delta G_{r,des}$	$\Delta F^{\neq}$	ΔF_r	$\Delta G_{r,des}$	$\Delta F^{\neq}$	ΔF_r	$\Delta G_{r,des}$
Case 1	**Static**	129.9	46.8	−2.8[a]	135.2	55.3	3.1[a]	87.2	−8.5	−58.0[a]
	US	111.4	−16.1	–	124.3	8.9	–	81.1	−62.5	–
	MTD	105.8	−2.1	–	142.6	10.9	–	86.4	−36.4	–
Case 2	**MTD**	82.4	0.4	–	148.0	67.5	–	73.4	−24.9	–
Case 3	**MTD**	71.5	−52.4	–	126.1	19.7	–	61.0	−58.8	–

[a] It should be noted that as long as the water is adsorbed within the zeolite pore, Helmholtz free energies are obtained, as the volume of the unit cell is kept constant (see Section 1.1 of the ESI), thus omitting the *pV* term. If the desorption of water is considered, a Gibbs free energy value is obtained as the gas phase accessible volume should be accounted for at the correct pressure.

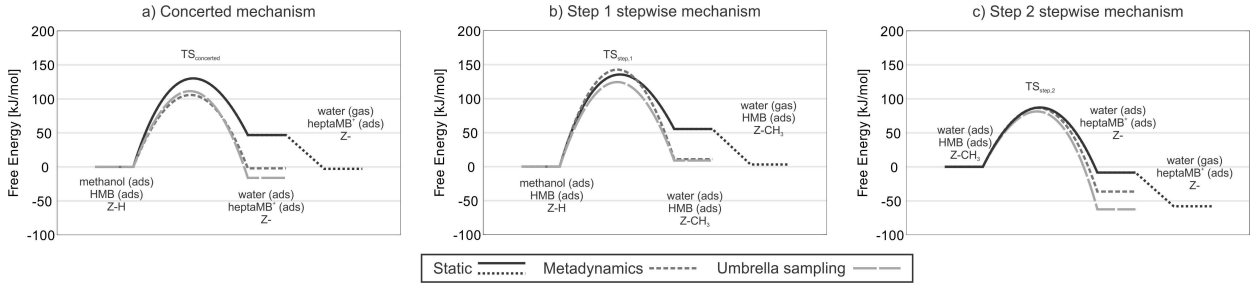

Figure 8. Free energy profile for the concerted (a) and step 1 (b) and step 2 (c) of the stepwise methylation of HMB at 623 K in Case 1 using static (full line), metadynamics (short-striped line) and umbrella sampling (long-striped line) simulations. For the static calculations, an extra desorption step of the formed water is taken into account (dotted line).

enhanced sampling molecular dynamics simulations is extremely challenging, certainly when the sampling has been performed based on first principle simulations which poses limits on the number of simulations and the length of the simulations that may be performed within a feasible computational time.[55] For the interested reader an estimate of the computational time used for the reactions under study has been given in Table S6 of the ESI. As reviewed earlier, the accuracy of the final results depends on the level of theory used to describe the system, the sampling protocol, and the estimator to obtain the free energy differences.[60,122–124] For DFT based reactions in zeolites only a few works are available which assess each of the components on the finally obtained free energies.[51,54,55]

3.2.1. Dynamic Versus Static Methods for Case 1 without Additional Water Molecules

To assess the influence of the dynamic approach on the direct and stepwise methylation routes, the simplest case (Case 1) where no additional water molecules are present is first discussed. The free energy results for Case 1 obtained via static, metadynamics, and umbrella sampling simulations are summarized in Figure 8 and Table 1. All results refer to the state where all species are adsorbed on the catalyst and thus intrinsic barriers are reported. As a result of the reaction, the heptamethylbenzenium cation and water are formed, which are both adsorbed in the cages of the zeolite. When water desorbs and is brought to the gas phase, entropy is gained. This state, which was evaluated based on the static results, is also shown on the figure. For the stepwise mechanism, the free energies are the result of two subsequent umbrella/metadynamics simulations and thus one must be careful in connecting the product state of the first step with the reactant of the next step. More information on this aspect is given further in this section.

The static free energy barriers together with a more detailed analysis of the influence of temperature on all static results and comparison of the static results with literature data can be found in Section 2 of the ESI. In general, our static calculations suggest that the stepwise mechanism becomes more important at higher temperatures, though the temperature range differs with the work of Brogaard and co-workers,[43] and suggest higher temperature ranges similarly to the results found in ref. [44].

At first instance, it is interesting to compare the static and the dynamic results for the concerted methylation step. The most pronounced effect of the dynamic sampling is observed on the stabilization of the products, where water is still co-adsorbed, which are substantially lower in free energy when using advanced dynamic methods. This can be ascribed to the different description of the mobility of the formed water, as revealed by the RDFs for the pairs formed by (i) the carbon and (ii) oxygen of methanol, shown in Figure 9. These RDFs indicate that the water molecules in the product state exhibit a substantial configurational freedom, shown by the broadly

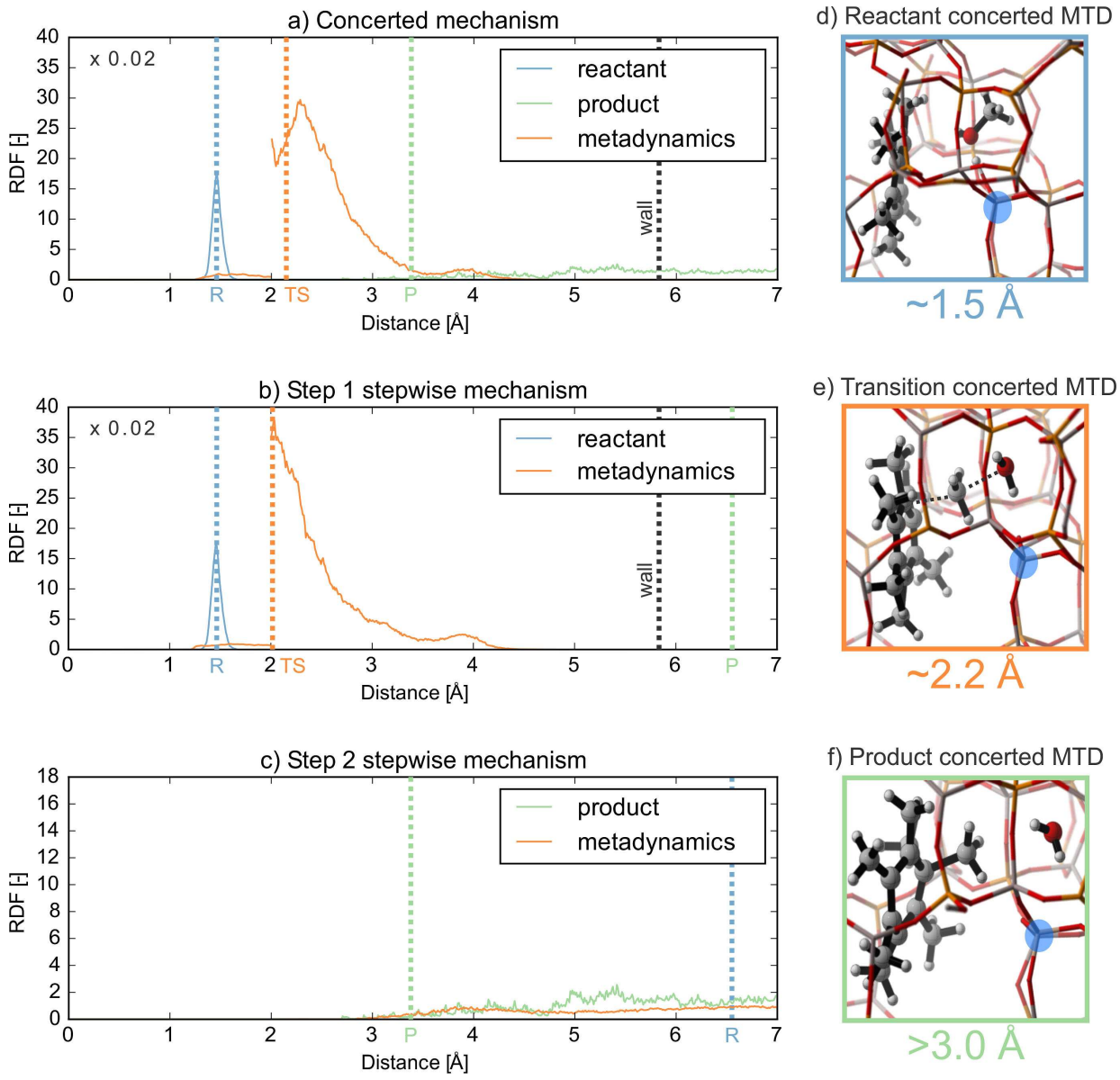

Figure 9. Radial distribution functions for the pairs formed by (i) the methyl group and (ii) the oxygen of the methanol molecule from MD runs in the reactant (blue) and product (green) state as well as for the MTD simulation (orange) for Case 1. These RDFs are calculated for the concerted methylation (a) and both step 1 (b) and step 2 (c) of the stepwise mechanism. Furthermore, the measured distances in the reactant (R), product (P) and different transition states (TS) calculated statically are added as dotted lines. The static value for the transition state of step 2 of the stepwise mechanism could not be added, as it attained a value of 8.7 Å, thus higher than the maximum used in the RDFs. Lastly, the position of the wall limiting the diffusion of the formed water to enhance recrossing in the MTD simulation is added. The first peak (at distances below 2 Å) is scaled down by a factor of 50 to improve visualization. Three snapshots of the reactant (d), transition (e) and product (f) states sampled in the metadynamics simulations of the concerted mechanism are added, with typical distances between the methyl group and the oxygen of the methanol indicated. In these snapshots, hydrogen is white, carbon is silver, oxygen is red, aluminum is grey, the silicon substitution is indicated in blue and phosphorus is orange.

smeared probability. This is confirmed by the RDFs for the pairs formed by (i) the oxygens of the BAS and (ii) all protons, depicted in Figure S26 and Figure S27 in the ESI. This configurational freedom is poorly accounted for by the static methods, employing a harmonic oscillator approximation in only one static point, indicated by the green dotted lines in Figure 9. By accounting for this configurational freedom using dynamic simulations, the product state is stabilized entropically in line with the lower free energies of the co-adsorbed products in Figure 8. The reaction free energy in the umbrella sampling simulations is slightly lower compared to the MTD simulations, which might be ascribed to the walls imposed in the metadynamics simulations to enhance recrossing as described in Section 2.4.1 and Section 1.4 of the ESI. While this wall does affect the regions of the phase space that can be explored, its location was chosen so to minimally affect the metadynamics simulation. As can be observed from Figure 9, the wall is indeed located far inside the product region, at a point where the RDF

determined from metadynamics for the pairs formed by (i) the methyl group and (ii) the oxygen of the methanol molecule is vanishingly small. In general, it is rather challenging to sample the product state where water diffuses quickly away from the active site into the pores of the zeolites. In this sense the product state is less well defined compared to the reactant state which is quite similar for all methods, as the discussion of Figure 6 demonstrated that methanol is fixed on the BAS in all cases (see Figure 9d). Irrespective of the errors induced by the sampling procedure (see Section 1.6 of the ESI for more information), the geometrical analysis and the obtained free energies clearly show that the mobility of the co-adsorbed water is insufficiently described by the static methods, which only consider one point on the free energy surface.

In a next step, it is interesting to study in how far similar effects are observed for the stepwise mechanism. Note that water is released after the first step in the stepwise mechanism. In our dynamic simulations, we opted to keep the water in the pores of the material. However, it was observed that water diffuses quickly to a neighboring cage. For the static simulations we investigated in how far the barriers of the second step are affected by removing water after step 1. As discussed in Section 2.2 of the ESI, the effect on the barrier is minimal. The dynamic results of the stepwise mechanism are the result of two enhanced sampling MD simulations where in the first set of simulations CV1 and CV3 are used and in the second step CV2 and CV3 are used, as schematically shown in Figure 4. To directly investigate the competition between the direct and stepwise mechanism from MD simulations, it is necessary to perform MTD or US simulations with a fixed set of the three collective variables, as this would allow to sample all possible steps, namely the methoxide formation (CV3), the carbon-carbon bond formation (CV2) and the carbon-oxygen breakage (CV1) all in the same run. Such study was performed in reference [52]. However, as the simulation time scales exponentially with the number of collective variables,[63] it was impossible to perform these simulations within this work. Furthermore, it was pointed out by De Wispelaere et al.[44,52] that no reaction free energies could be obtained from the 3D MTD simulations, as the product region was insufficiently sampled.

When comparing the static versus the dynamic results for the first step, a similar stabilization of the formed products, i.e. the methoxide formation and the co-adsorbed water, are observed compared to the static results. Also for step 2 the products before desorption of water are substantially stabilized in the dynamic simulations compared to the static results. It was statically observed that for the product state of step 2, the water molecule is stabilized through a hydrogen bond with the negatively charged framework, thereby losing a large portion of its entropy in this step, as depicted in Figure S10 of the ESI. In the dynamic simulations, water remains diffusive. Finally, it is important to note that one cannot connect the product of step 1 and reactant of step 2 directly as the two states have been obtained from biased MD simulations with different collective variables. More information is given in the ESI, Section 4.

The overall free energy barriers obtained with all methods show similar trends given the numerical inaccuracies and sampling errors. A more detailed explanation regarding the errors on the various methods is given in Section 1.6 of the ESI. Rather large differences are obtained for the free energy barrier of the methoxide formation obtained with the MTD and US methods. Our error analysis shows that the sampling error on the US simulations is larger for the here conducted results. Further analysis demonstrates that the US simulations only sample one type of transition state, which is assisted by the presence of the HMB, whereas in MTD broader regions of the phase space were sampled accounting for an assisted and non-assisted transition state. If the sampling were to be sufficient, both methods should sample similar regions of phase space. However, even after an excessive number of simulations, our simulations show that it is very challenging to obtain similar barriers. More information can be found in Section 1.5 and 1.6 of the ESI. For the current study focus is not to calculate the most accurate free energy barriers, instead we wanted to obtain important trends regarding the role of water on the methylation of HMB.

Qualitatively, the dynamic results of Case 1 lead to a similar conclusion as the static methodology discussed in Section 2 of the ESI, namely that the concerted and stepwise mechanisms are competitive at 623 K, though the concerted will prevail due to the high barrier for methoxide formation. Furthermore, the dynamic results highlight the importance of the release of water in this process.

For the more complicated cases (Case 2 and 3), where more guest molecules are present in the pores of the material, only enhanced sampling MD techniques are used. Based on previous findings and the fact that less prior knowledge on the reaction path is needed within metadynamics, we opted to further use metadynamics in Case 2 and 3.[125]

3.2.2. Influence of the Protic Environment in Case 2 and 3

In a next step, we want to elucidate the role of additional protic molecules present in the catalyst by comparing the methylation free energies in Case 2 and 3. The free energy profiles obtained using metadynamics, which are also listed in Table 1, are presented in Figure 10.

The profiles show that the concerted mechanism prevails in all cases. Furthermore, comparison of both profiles shows that the presence of additional protic molecules lowers all barriers and stabilizes the intermediate and product states. The stabilization of the intermediate and product state can be explained by the stabilization of the formed water in the protonated water network. This effect is more pronounced at higher water content.

The decreased barriers for the concerted methylation and methoxide formation due to the assistance of protic molecules, shown in earlier work,[13,41,44] is confirmed here and originates from the formation of solvation shells as already introduced earlier for the reactant valley in Figure 6. Recalculating these RDFs for the metadynamics of these two reactions runs confirms the existence of these shells as shown in Figure 11a and b. As the intensity of the peak between 3.1 Å and 3.5 Å

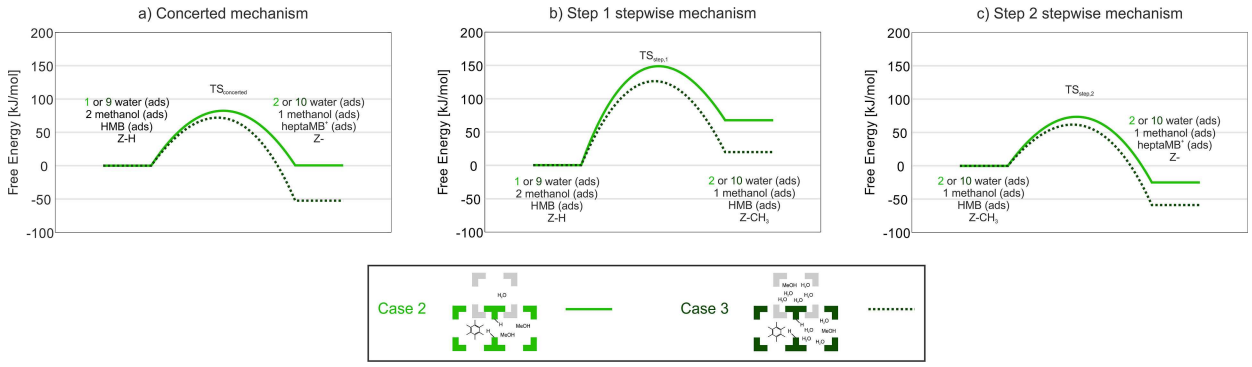

Figure 10. Free energy profile for the concerted (a) and step 1 (b) and step 2 (c) of the stepwise methylation of HMB at 623 K at higher guest molecule loadings and acid site density, namely Case 2 (full line) and Case 3 (dotted line) obtained with metadynamics. The reference level for the reactants in both cases has been assumed zero, however in Case 2 one water molecule was adsorbed, whereas in Case 3 nine water molecules were adsorbed in the unit cell. The obtained barriers are thus intrinsic energy barriers compared to the state in which all molecules are already adsorbed.

increases when going from Case 2 to Case 3, the elevated water content in the latter case leads to an increased solvation shell formation and thus increased assistance compared to Case 2. Furthermore, a detailed visual analysis of the transition states shows that for Case 3 the transition state is efficiently stabilized by the surrounding molecules. For Case 2 on the other hand, the concentration of assisting molecules is too low and both assisted and unassisted transition states are sampled, as depicted in the snapshots for Figure 11a. Similar snapshots for the methoxide formation are provided in Figure S15 of the ESI. The decreased assistance leads to higher barriers in Case 2, which is in line with earlier work.[13]

Also for the second step of the stepwise mechanism, a lower free energy barrier is observed when increasing the water content. This can be explained by a stabilization of the BASs with the surrounding protic molecules, though not as straightforwardly as for the concerted methylation and methoxide formation. To this end, the RDFs for the pairs formed by (i) all protons and (ii) the oxygens of the BAS are shown for Case 2 and Case 3 in Figure 12. For the metadynamics and product state simulations of Case 3, these RDFs reveal an additional peak between 1.8 and 2.25 Å compared to Case 2. As shown in the snapshots in Figure 12b, the protic molecules stabilize the unprotonated BAS, which is formed from the methoxide, by a protonated water cluster resembling the Grotthuss mechanism for Case 3.[126] The distances of the hydrogen bonds formed in this chain are within the range of 1.8 and 2.25 Å, thus corresponding to this peak. When considering Case 2, insufficient protic molecules seem to be present to stabilize the unprotonated BAS and thus fail to lower the transition state barrier.

As assistance by the additional water molecules thus explains the decreased barriers and stabilized products between Case 2 and Case 3, this study shows that not only competitive adsorption between methanol and water[13] needs to be considered when clarifying the enhanced conversion of methanol in the presence of water.[11,19,127,128] The assisting role of water might have an important effect on the whole reaction profile and a study on its effect on the complete aromatics mechanism might lead to new insights on the problem at hand.

4. Conclusions

In this work, new insights on the influence of protic molecules on the methylation of hexamethylbenzene (HMB) in H-SAPO-34 were obtained using dynamic first principle techniques. To this end, the competitive concerted and stepwise methylation mechanisms were studied for three cases with an increasing amount of protic molecules and an increasing amount of BASs. The simulations are performed using first principle molecular dynamics methods to account for entropic and dynamic effects at elevated temperatures.

First, the influence of the protic environment on the adsorption of the reactants in the catalyst pores was investigated. It was observed that HMB adopts a preferred position oriented along the z-axis (the longest direction of the cage) with the π-clouds oriented to the BAS for Case 1 and Case 2. In Case 3, at a higher water content, the orientation of the π-clouds to the BAS was screened by the adsorbed protic molecules, which also offered new stabilizing interactions for the π-clouds. Furthermore, higher water loadings lead to the formation of solvation shells around methanol in Case 3, thus allowing for the proton donation from the BAS to methanol to occur by another protic molecule. Nevertheless, the protic environment did not significantly influence the pre-reactive complex formation as methanol mostly oriented its methyl group away from the HMB in all cases.

Subsequently, the competition between the concerted and stepwise mechanisms was analyzed by calculating the free energy barriers for all elementary reaction steps. In general, the results demonstrated that the concerted mechanism prevails at the reaction conditions studied in this work. Furthermore, two main influences on the free energy barriers and the reaction free energies could be distinguished.

First, the effect of static versus enhanced sampling MD methods was tested for Case 1. The main difference between

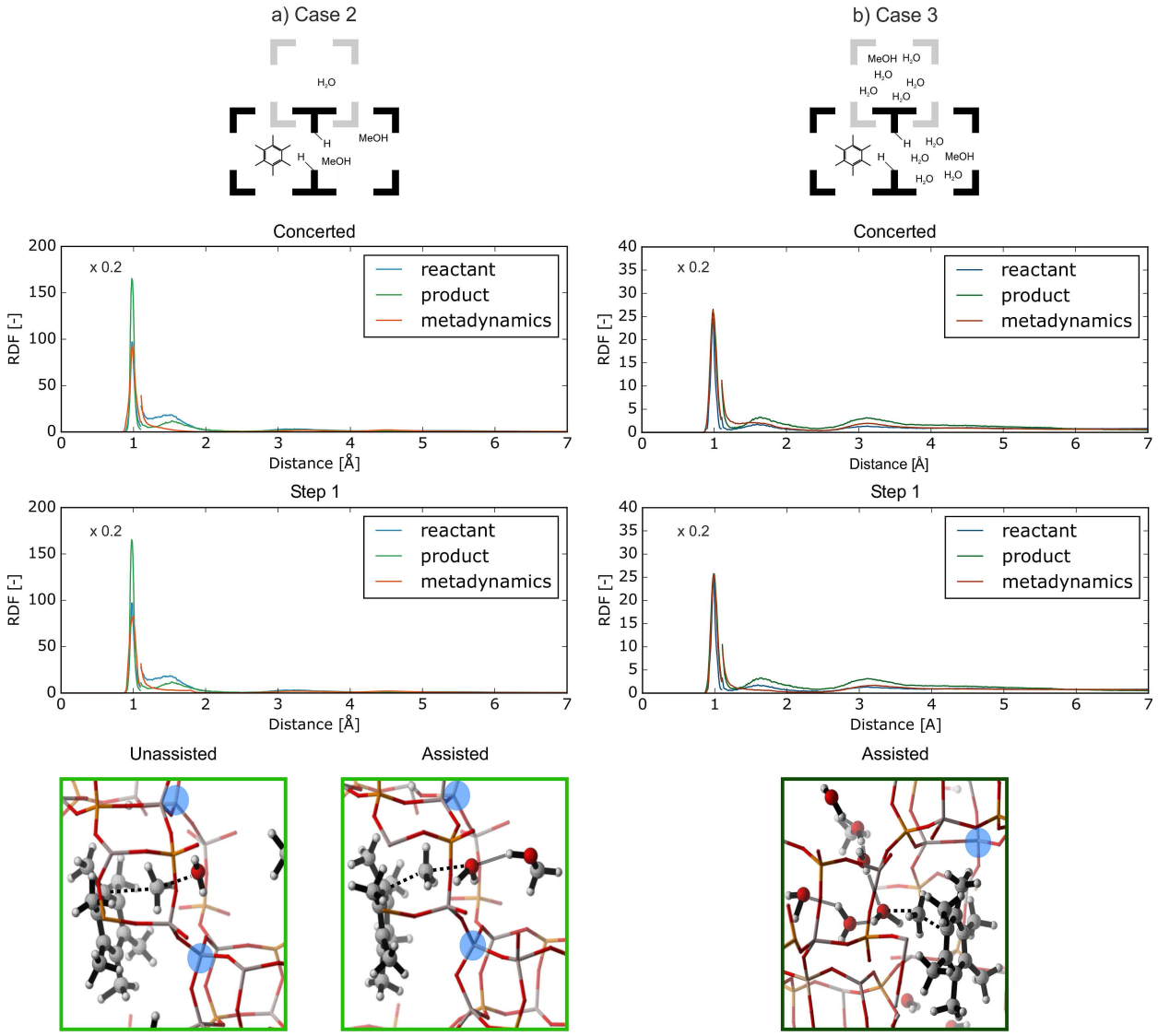

Figure 11. Radial distribution function for the pairs formed by (i) all protons and (ii) the oxygens of the methanol molecules from MD runs in the reactant and product state as well as during the MTD simulations for the concerted methylation (top) and methoxide formation (middle) for Case 2 (a) and Case 3 (b). Furthermore, the unassisted and assisted transition states are visualized in the snapshots at the bottom. The first peaks of the RDFs (at distances below about 1.1 Å) are scaled down by a factor of 5 to improve visualization. In these snapshots, hydrogen is white, carbon is silver, oxygen is red, aluminum is grey, the silicon substitution is indicated in blue and phosphorus is orange.

the results obtained from the enhanced sampling methods and the static simulation methods was observed for the stabilization of the products in which water was formed. In the case of dynamic methods, the water formed in the methylation step becomes rather mobile, which yields an entropic stabilization of the product region. In static methods, this configurational freedom is not properly described as only one point is considered on the free energy surface. The radial distribution function between the carbon and oxygen of methanol showed a substantial diffusional freedom of water in the product state, which cannot be captured statically. Apart from these qualitative observations, our results also show that obtaining accurate free energy barriers and reaction free energies from biased molecular dynamics simulation methods remains very challenging. An exhaustive number of simulations are necessary to obtain converged free energies along the reaction coordinate. A detailed comparison of various enhanced sampling methods and the impact of collective variables on the results would be interesting for future studies.

Second, by comparing the more complex Case 2 and Case 3, the effect of additional protic molecules in the catalyst pores could be unraveled. In all cases, decreased barriers and additional stabilization of the products was observed. The decreased barrier for the concerted methylation and methoxide formation and the stabilization of the product could be associated to the solvation shells that are more prominent in Case 3. Furthermore, a stabilization of the deprotonated BAS formed in the second step of the stepwise mechanism occurred by a Grotthuss-type mechanism linking both BASs. This effect leads to a decreased barrier for this second step in Case 3.

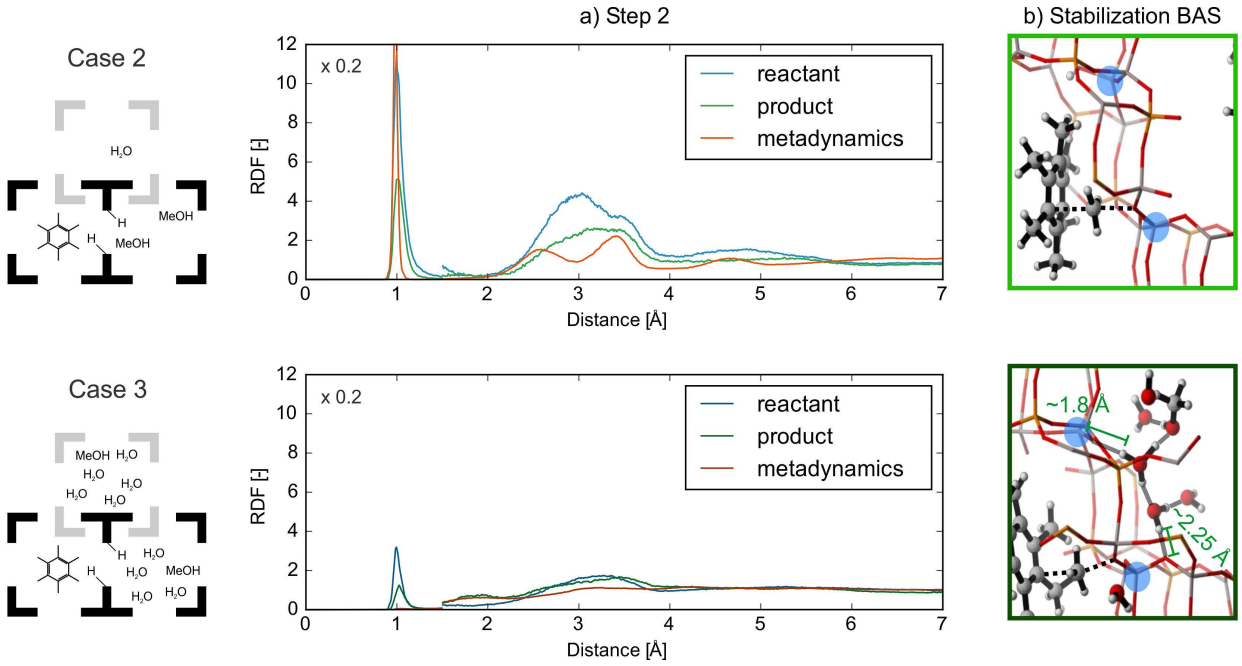

Figure 12. Radial distribution function for the pairs formed by (i) all protons and (ii) the oxygens of the Brønsted acid sites from MD runs in the reactant and product state as well as during the MTD simulations for the second step of the stepwise mechanism (a) for Case 2 (top) and Case 3 (bottom). Furthermore, a snapshot of the BAS during the transition state is shown to depict the stabilization of the formed deprotonated BAS by the protic molecules present (b). The first peaks of the RDFs (at distances below about 1.3 Å) are scaled down by a factor of 5 to improve visualization. In these snapshots, hydrogen is white, carbon is silver, oxygen is red, aluminum is grey, the silicon substitution is indicated in blue and phosphorus is orange.

In conclusion, our results highlight the importance of correctly accounting for the dynamic and assisting behavior of the protic environment within zeolite catalysis at process conditions. Therefore, the use of advanced molecular dynamics to further unravel the reaction mechanism governing the MTO process is indispensable.

Acknowledgements

V.V.S. and S.B. acknowledge funding from the European Union's Horizon 2020 research and innovation program (consolidator ERC grant agreement No. 647755 – DYNPOR (2015-2020)). S.M.J.R and L.V. acknowledge the Fund for Scientific Research Flanders (FWO) for their postdoctoral fellowships. V.V.S. acknowledges the Research Board of the Ghent University (BOF). The computational resources and services used were provided by Ghent University (Stevin Supercomputer Infrastructure), the VSC (Flemish Supercomputer Center), funded by the Research Foundation – Flanders (FWO).

Conflict of Interest

The authors declare no conflict of interest.

Keywords: density functional theory · enhanced sampling · H-SAPO-34 · methylation · water

[1] R. W. Bentley, *Energy Policy* **2002**, *30*, 189–205.
[2] A. Corma, S. Iborra, A. Velty, *Chem. Rev.* **2007**, *107*, 2411–2502.
[3] C. Briens, J. Piskorz, F. Berruti, *Int. J. Chem. React. Eng.* **2008**, *6*, R2.
[4] P. Sudarsanam, R. Zhong, S. V. den Bosch, S. M. Coman, V. I. Parvulescu, B. F. Sels, *Chem. Soc. Rev.* **2018**, *47*, 8349–8402.
[5] P. L. Spath, D. C. Dayton, **2003**, DOI: 10.2172/15006100.
[6] F. L. Bleken, S. Chavan, U. Olsbye, M. Boltz, F. Ocampo, B. Louis, *Appl. Catal. A* **2012**, *447–448*, 178–185.
[7] S. Abrol, C. M. Hilton, *Comput. Chem. Eng.* **2012**, *40*, 117–131.
[8] U. Olsbye, S. Svelle, M. Bjørgen, P. Beato, T. V. W. Janssens, F. Joensen, S. Bordiga, K. P. Lillerud, *Angew. Chem. Int. Ed.* **2012**, *51*, 5810–5831.
[9] K. Hemelsoet, J. Van der Mynsbrugge, K. De Wispelaere, M. Waroquier, V. Van Speybroeck, *ChemPhysChem* **2013**, *14*, 1526–1545.
[10] I. Yarulina, A. D. Chowdhury, F. Meirer, B. M. Weckhuysen, J. Gascon, *Nat. Catal.* **2018**, *1*, 398–411.
[11] J. Q. Chen, A. Bozzano, B. Glover, T. Fuglerud, S. Kvisle, *Catal. Today* **2005**, *106*, 103–107.
[12] K. De Wispelaere, K. Hemelsoet, M. Waroquier, V. Van Speybroeck, *J. Catal.* **2013**, *305*, 76–80.
[13] K. De Wispelaere, C. S. Wondergem, B. Ensing, K. Hemelsoet, E. J. Meijer, B. M. Weckhuysen, V. Van Speybroeck, J. Ruiz-Martínez, *ACS Catal.* **2016**, 1991–2002.
[14] B. P. C. Hereijgers, F. Bleken, M. H. Nilsen, S. Svelle, K.-P. Lillerud, M. Bjørgen, B. M. Weckhuysen, U. Olsbye, *J. Catal.* **2009**, *264*, 77–87.
[15] M. Yang, P. Tian, C. Wang, Y. Yuan, Y. Yang, S. Xu, Y. He, Z. Liu, *Chem. Commun.* **2014**, *50*, 1845–1847.
[16] T. Álvaro-Muñoz, C. Márquez-Álvarez, E. Sastre, *Catal. Today* **2012**, *179*, 27–34.
[17] T. Álvaro-Muñoz, C. Márquez-Álvarez, E. Sastre, *Appl. Catal. A* **2014**, *472*, 72–79.
[18] L. Wu, E. J. M. Hensen, *Catal. Today* **2014**, *235*, 160–168.
[19] A. J. Marchi, G. F. Froment, *Appl. Catal.* **1991**, *71*, 139–152.
[20] X. Wu, R. G. Anthony, *Appl. Catal. A* **2001**, *218*, 241–250.
[21] W. Song, H. Fu, J. F. Haw, *J. Am. Chem. Soc.* **2001**, *123*, 4749–4754.
[22] M. Shahda, Y. Dengchao, W. Huixin, *Pet. Sci. Technol.* **2008**, *26*, 1893–1903.
[23] A. Taheri Najafabadi, S. Fatemi, M. Sohrabi, M. Salmasi, *J. Ind. Eng. Chem.* **2012**, *18*, 29–37.

[24] S. Tjandra, R. G. Anthony, A. Akgerman, *Ind. Eng. Chem. Res.* **1993**, *32*, 2602–2607.
[25] X. Yin, D. Y. C. Leung, J. Chang, J. Wang, Y. Fu, C. Wu, *Energy Fuels* **2005**, *19*, 305–310.
[26] A. Demirbas, *Prog. Energy Combust. Sci.* **2007**, *33*, 1–18.
[27] J. F. Haw, D. M. Marcus, *Top. Catal.* **2005**, *34*, 41–48.
[28] V. Van Speybroeck, K. De Wispelaere, J. Van der Mynsbrugge, M. Vandichel, K. Hemelsoet, M. Waroquier, *Chem. Soc. Rev.* **2014**, *43*, 7326–7357.
[29] A. D. Chowdhury, A. L. Paioni, K. Houben, G. T. Whiting, M. Baldus, B. M. Weckhuysen, *Angew. Chem. Int. Ed.* **2018**, *57*, 8095–8099.
[30] J. F. Haw, W. Song, D. M. Marcus, J. B. Nicholas, *Acc. Chem. Res.* **2003**, *36*, 317–326.
[31] I. M. Dahl, S. Kolboe, *Catal. Lett.* **1993**, *20*, 329–336.
[32] I. M. Dahl, S. Kolboe, *J. Catal.* **1994**, *149*, 458–464.
[33] I. M. Dahl, S. Kolboe, *J. Catal.* **1996**, *161*, 304–309.
[34] J. Van der Mynsbrugge, M. Visur, U. Olsbye, P. Beato, M. Bjørgen, V. Van Speybroeck, S. Svelle, *J. Catal.* **2012**, *292*, 201–212.
[35] D. Lesthaeghe, B. De Sterck, V. Van Speybroeck, G. B. Marin, M. Waroquier, *Angew. Chem. Int. Ed.* **2007**, *46*, 1311–1314.
[36] V. Van Speybroeck, K. Hemelsoet, K. De Wispelaere, Q. Qian, J. Van der Mynsbrugge, B. De Sterck, B. M. Weckhuysen, M. Waroquier, *ChemCatChem* **2013**, *5*, 173–184.
[37] K. Hemelsoet, Q. Qian, T. De Meyer, K. De Wispelaere, B. De Sterck, B. M. Weckhuysen, M. Waroquier, V. Van Speybroeck, *Chem. Eur. J.* **2013**, *19*, 16595–16606.
[38] I. I. Ivanova, A. Corma, *J. Phys. Chem. B* **1997**, *101*, 547–551.
[39] S. Svelle, S. Kolboe, U. Olsbye, O. Swang, *J. Phys. Chem. B* **2003**, *107*, 5251–5260.
[40] S. Svelle, M. Visur, U. Olsbye, Saepurahman, M. Bjørgen, *Top. Catal.* **2011**, *54*, 897–906.
[41] J. Van der Mynsbrugge, S. L. C. Moors, K. De Wispelaere, V. Van Speybroeck, *ChemCatChem* **2014**, *6*, 1906–1918.
[42] A. M. Vos, K. H. L. Nulens, F. De Proft, R. A. Schoonheydt, P. Geerlings, *J. Phys. Chem. B* **2002**, *106*, 2026–2034.
[43] R. Y. Brogaard, R. Henry, Y. Schuurman, A. J. Medford, P. G. Moses, P. Beato, S. Svelle, J. K. Nørskov, U. Olsbye, *J. Catal.* **2014**, *314*, 159–169.
[44] K. De Wispelaere, S. Bailleul, V. Van Speybroeck, *Catal. Sci. Technol.* **2016**, *6*, 2686–2705.
[45] K. De Wispelaere, J. S. Martínez-Espín, M. J. Hoffmann, S. Svelle, U. Olsbye, T. Bligaard, *Catal. Today* **2018**, *312*, 35–43.
[46] M. Westgård Erichsen, K. De Wispelaere, K. Hemelsoet, S. L. C. Moors, T. Deconinck, M. Waroquier, S. Svelle, V. Van Speybroeck, U. Olsbye, *J. Catal.* **2015**, *328*, 186–196.
[47] A. J. Jones, E. Iglesia, *Angew. Chem. Int. Ed.* **2014**, *53*, 12177–12181.
[48] T. Maihom, B. Boekfa, J. Sirijaraensre, T. Nanok, M. Probst, J. Limtrakul, *J. Phys. Chem. C* **2009**, *113*, 6654–6662.
[49] M. N. Mazar, S. Al-Hashimi, A. Bhan, M. Cococcioni, *J. Phys. Chem. C* **2012**, *116*, 19385–19395.
[50] L. Benco, T. Bučko, J. Hafner, *J. Catal.* **2011**, *277*, 104–116.
[51] T. Bučko, L. Benco, J. Hafner, J. G. Ángyán, *J. Catal.* **2011**, *279*, 220–228.
[52] K. De Wispelaere, B. Ensing, A. Ghysels, E. J. Meijer, V. Van Speybroeck, *Chem. Eur. J.* **2015**, *21*, 9385–9396.
[53] T. Bučko, J. Hafner, *J. Catal.* **2015**, *329*, 32–48.
[54] T. Bučko, S. Chibani, J.-F. Paul, L. Cantrel, M. Badawi, *Phys. Chem. Chem. Phys.* **2017**, *19*, 27530–27543.
[55] J. Rey, A. Gomez, P. Raybaud, C. Chizallet, T. Bučko, *J. Catal.* **2019**, *373*, 361–373.
[56] C. Abrams, G. Bussi, *Entropy* **2013**, *16*, 163–199.
[57] T. Bučko, *J. Phys. Condens. Matter* **2008**, *20*, 064211.
[58] D. Trzesniak, A.-P. E. Kunz, W. F. van Gunsteren, *ChemPhysChem* **2007**, *8*, 162–169.
[59] D. Frenkel, B. Smit, *Understanding Molecular Simulation: From Algorithms to Applications*, Academic Press, **2001**.
[60] C. D. Christ, A. E. Mark, W. F. van Gunsteren, *J. Comput. Chem.* **2010**, *31*, 1569–1582.
[61] A. Laio, M. Parrinello, *Proc. Mont. Acad. Sci.* **2002**, *99*, 12562–12566.
[62] M. Iannuzzi, A. Laio, M. Parrinello, *Phys. Rev. Lett.* **2003**, *90*, 238302.
[63] A. Laio, F. L. Gervasio, *Rep. Prog. Phys.* **2008**, *71*, 126601.
[64] G. M. Torrie, J. P. Valleau, *Chem. Phys. Lett.* **1974**, *28*, 578–581.
[65] G. M. Torrie, J. P. Valleau, *J. Comput. Phys.* **1977**, *23*, 187–199.
[66] J. Kästner, *Wiley Interdiscip. Rev.: Comput. Mol. Sci.* **2011**, *1*, 932–942.
[67] S. L. C. Moors, K. De Wispelaere, J. Van der Mynsbrugge, M. Waroquier, V. Van Speybroeck, *ACS Catal.* **2013**, *3*, 2556–2567.
[68] L. Vanduyfhuys, A. Ghysels, S. M. J. Rogge, R. Demuynck, V. Van Speybroeck, *Mol. Simul.* **2015**, *41*, 1311–1328.
[69] D. H. Olson, W. O. Haag, W. S. Borghard, *Microporous Mesoporous Mater.* **2000**, *35–36*, 435–446.
[70] D. H. Olson, W. O. Haag, R. M. Lago, *J. Catal.* **1980**, *61*, 390–396.
[71] H. Nakamoto, H. Takahashi, *Zeolites* **1982**, *2*, 67–68.
[72] T. Sano, T. Kasuno, K. Takeda, S. Arazaki, Y. Kawakami, in *Stud. Surf. Sci. Catal.* (Eds.: H. Chon, S.-K. Ihm, Y. S. Uh), Elsevier, **1997**, pp. 1771–1778.
[73] S. Eckstein, P. H. Hintermeier, R. Zhao, E. Baráth, H. Shi, Y. Liu, J. A. Lercher, *Angew. Chem. Int. Ed.* **2019**, *58*, 3450–3455.
[74] V. Termath, F. Haase, J. Sauer, J. Hutter, M. Parrinello, *J. Am. Chem. Soc.* **1998**, *120*, 8512–8516.
[75] G. Sastre, D. W. Lewis, C. R. A. Catlow, *J. Phys. Chem.* **1996**, *100*, 6722–6730.
[76] "Database of Zeolite Structures," can be found under http://www.iza-structure.org/databases/.
[77] C.-M. Wang, Y.-D. Wang, Y.-J. Du, G. Yang, Z.-K. Xie, *Catal. Sci. Technol.* **2015**, *5*, 4354–4364.
[78] M. Nielsen, R. Y. Brogaard, H. Falsig, P. Beato, O. Swang, S. Svelle, *ACS Catal.* **2015**, *5*, 7131–7139.
[79] T. F. Willems, C. H. Rycroft, M. Kazi, J. C. Meza, M. Haranczyk, *Microporous Mesoporous Mater.* **2012**, *149*, 134–141.
[80] D. W. H. Rankin, *Crystallogr. Rev.* **2009**, *15*, 223–224.
[81] J. Kuhn, J. M. Castillo-Sanchez, J. Gascon, S. Calero, D. Dubbeldam, T. J. H. Vlugt, F. Kapteijn, J. Gross, *J. Phys. Chem. C* **2009**, *113*, 14290–14301.
[82] S. M. J. Rogge, R. Goeminne, R. Demuynck, J. J. Gutiérrez-Sevillano, S. Vandenbrande, L. Vanduyfhuys, M. Waroquier, T. Verstraelen, V. Van Speybroeck, *Adv. Theory Simul.* **2019**, *2*, 1800177.
[83] G. Kresse, J. Hafner, *Phys. Rev. B* **1993**, *47*, 558–561.
[84] G. Kresse, J. Hafner, *Phys. Rev. B* **1994**, *49*, 14251–14269.
[85] G. Kresse, J. Furthmüller, *Comput. Mater. Sci.* **1996**, *6*, 15–50.
[86] G. Kresse, J. Furthmüller, *Phys. Rev. B* **1996**, *54*, 11169–11186.
[87] J. Hajek, J. Van der Mynsbrugge, K. De Wispelaere, P. Cnudde, L. Vanduyfhuys, M. Waroquier, V. Van Speybroeck, *J. Catal.* **2016**, *340*, 227–235.
[88] J. Hajek, B. Bueken, M. Waroquier, D. De Vos, V. Van Speybroeck, *ChemCatChem* **2017**, *9*, 2203–2210.
[89] P. Cnudde, K. De Wispelaere, J. Van der Mynsbrugge, M. Waroquier, V. Van Speybroeck, *J. Catal.* **2017**, *345*, 53–69.
[90] I. Yarulina, K. De Wispelaere, S. Bailleul, J. Goetze, M. Radersma, E. Abou-Hamad, I. Vollmer, M. Goesten, B. Mezari, E. J. M. Hensen, J. S. Martínez-Espín, M. Morten, S. Mitchell, J. Perez-Ramirez, U. Olsbye, B. M. Weckhuysen, V. Van Speybroeck, F. Kapteijn, J. Gascon, *Nat. Chem.* **2018**, *10*, 804–812.
[91] K. Yang, J. Zheng, Y. Zhao, D. G. Truhlar, *J. Chem. Phys.* **2010**, *132*, 164117.
[92] P. E. Blöchl, *Phys. Rev. B* **1994**, *50*, 17953–17979.
[93] G. Kresse, D. Joubert, *Phys. Rev. B* **1999**, *59*, 1758–1775.
[94] S. Grimme, J. Antony, S. Ehrlich, H. Krieg, *J. Chem. Phys.* **2010**, *132*, 154104.
[95] N. Hansen, T. Kerber, J. Sauer, A. T. Bell, F. J. Keil, *J. Am. Chem. Soc.* **2010**, *132*, 11525–11538.
[96] S. Svelle, C. Tuma, X. Rozanska, T. Kerber, J. Sauer, *J. Am. Chem. Soc.* **2009**, *131*, 816–825.
[97] V. Van Speybroeck, J. Van der Mynsbrugge, M. Vandichel, K. Hemelsoet, D. Lesthaeghe, A. Ghysels, G. B. Marin, M. Waroquier, *J. Am. Chem. Soc.* **2011**, *133*, 888–899.
[98] G. Piccini, M. Alessio, J. Sauer, *Angew. Chem. Int. Ed.* **2016**, *55*, 5235–5237.
[99] H. Eshuis, J. E. Bates, F. Furche, *Theor. Chem. Acc.* **2012**, *131*, 1084.
[100] F. Furche, *Phys. Rev. B* **2001**, *64*, 195120.
[101] J. Harl, G. Kresse, *Phys. Rev. Lett.* **2009**, *103*, 056401.
[102] Y. Zhao, D. G. Truhlar, *Acc. Chem. Res.* **2008**, *41*, 157–167.
[103] Y. Zhao, D. G. Truhlar, *J. Phys. Chem. C* **2008**, *112*, 4061–4067.
[104] Y. Zhao, D. G. Truhlar, *J. Chem. Theory Comput.* **2008**, *4*, 1849–1868.
[105] B. Boekfa, S. Choomwattana, P. Khongpracha, J. Limtrakul, *Langmuir* **2009**, *25*, 12990–12999.
[106] A. Heyden, A. T. Bell, F. J. Keil, *J. Chem. Phys.* **2005**, *123*, 224101.
[107] P. Pulay, *Chem. Phys. Lett.* **1980**, *73*, 393–398.
[108] W. H. Press, B. P. Flannery, S. A. Teukolsky, W. T. Vetterling, *Numerical Recipes: The Art of Scientific Computing*, Cambridge Univ. Press, New York, **1986**.
[109] B. A. De Moor, A. Ghysels, M.-F. Reyniers, V. Van Speybroeck, M. Waroquier, G. B. Marin, *J. Chem. Theory Comput.* **2011**, *7*, 1090–1101.

[110] K. De Wispelaere, L. Vanduyfhuys, V. Van Speybroeck, in *Model. Simul. Sci. Micro- Meso-Porous Mater.* (Eds.: C. R. A. Catlow, V. Van Speybroeck, R. A. van Santen), Elsevier, **2018**, pp. 189–228.
[111] A. Ghysels, T. Verstraelen, K. Hemelsoet, M. Waroquier, V. Van Speybroeck, *J. Chem. Inf. Model.* **2010**, *50*, 1736–1750.
[112] J. Hutter, M. Iannuzzi, F. Schiffmann, J. VandeVondele, *Wiley Interdiscip. Rev.: Comput. Mol. Sci.* **2014**, *4*, 15–25.
[113] J. VandeVondele, M. Krack, F. Mohamed, M. Parrinello, T. Chassaing, J. Hutter, *Comput. Phys. Commun.* **2005**, *167*, 103–128.
[114] G. J. Martyna, D. J. Tobias, M. L. Klein, *J. Chem. Phys.* **1994**, *101*, 4177–4189.
[115] G. Lippert, J. Hutter, M. Parrinello, *Mol. Phys.* **1997**, *92*, 477–488.
[116] G. Lippert, J. Hutter, M. Parrinello, *Theor. Chem. Acc.* **1999**, *103*, 124–140.
[117] S. Goedecker, M. Teter, J. Hutter, *Phys. Rev. B* **1996**, *54*, 1703–1710.
[118] T. Verstraelen, L. Vanduyfhuys, S. Vandenbrande, S. M. J. Rogge, "Yaff, Yet Another Force Field.," can be found under http://molmod.ugent.be/software/.
[119] S. Kumar, J. M. Rosenberg, D. Bouzida, R. H. Swendsen, P. A. Kollman, *J. Comput. Chem.* **1992**, *13*, 1011–1021.
[120] M. Souaille, B. Roux, *Comput. Phys. Commun.* **2001**, *135*, 40–57.
[121] M. Bonomi, D. Branduardi, G. Bussi, C. Camilloni, D. Provasi, P. Raiteri, D. Donadio, F. Marinelli, F. Pietrucci, R. A. Broglia, M. Parrinello, *Comput. Phys. Commun.* **2009**, *180*, 1961–1972.
[122] N. Hansen, W. F. van Gunsteren, *J. Chem. Theory Comput.* **2014**, *10*, 2632–2647.
[123] R. Demuynck, S. M. J. Rogge, L. Vanduyfhuys, J. Wieme, M. Waroquier, V. Van Speybroeck, *J. Chem. Theory Comput.* **2017**, *13*, 5861–5873.
[124] M. A. Cuendet, M. E. Tuckerman, *J. Chem. Theory Comput.* **2014**, *10*, 2975–2986.
[125] A. Barducci, M. Bonomi, M. Parrinello, *Wiley Interdiscip. Rev.: Comput. Mol. Sci.* **2011**, *1*, 826–843.
[126] D. Marx, *ChemPhysChem* **2006**, *7*, 1848–1870.
[127] A. J. Marchi, G. F. Froment, *Appl. Catal. A* **1993**, *94*, 91–106.
[128] W. Wang, A. Buchholz, M. Seiler, M. Hunger, *J. Am. Chem. Soc.* **2003**, *125*, 15260–15267.

Manuscript received: April 23, 2019
Revised manuscript received: June 5, 2019
Accepted manuscript online: June 25, 2019
Version of record online: July 9, 2019

